Diffuse x-ray scattering from inclusions in ferromagnetic $Ge_{1-x}Mn_x$ layers

V. Holý,[1] R. T. Lechner,[2] S. Ahlers,[3] L. Horák,[1] T. H. Metzger,[4] A. Navarro-Quezada,[2] A. Trampert,[5] D. Bougeard,[3] and G. Bauer[2]

[1]*Faculty of Mathematics and Physics, Charles University, Ke Karlovu 5, 121 16 Prague, Czech Republic*

[2]*Institut für Halbleiter- und Festkörperphysik, Johannes Kepler Universität Linz, 4040 Linz, Austria*

[3]*Walter Schottky Institut, Technische Universität München, Am Coulombwall 3, D-85748 Garching, Germany*

[4]*ESRF, 6 rue Jules Horowitz, B.P. 220, F-38043 Grenoble Cedex, France*

[5]*P. Drude Institut für Festkörperelektronik, Hausvogteipl. 5-7, D-10117 Berlin, Germany*

(Received 29 May 2008; revised manuscript received 8 August 2008; published 2 October 2008)

Magnetic properties of $Ge_{1-x}Mn_x$ epitaxial layers with a Mn content of a few percents are substantially influenced by inhomogeneities in the distribution of Mn atoms in the Ge lattice. Depending on the substrate temperature during molecular-beam epitaxial fabrication, apparently cubic, coherent Mn-rich clusters or incoherent precipitates consisting of the hexagonal, intermetallic Mn_5Ge_3 phase can occur in a defect free, diamond lattice Ge matrix. In this work, we apply synchrotron x-ray diffraction in grazing-incidence geometry to probe the diffuse scattered intensity of the distorted Ge host lattice. Based on a theoretical description of the scattered intensity we derive quantitative information on the lattice mismatch between the Mn inclusions and the Ge lattice, as well as on the average size of the inclusions and the average Mn content within the inclusions.

DOI: 10.1103/PhysRevB.78.144401 PACS number(s): 75.50.Pp, 61.05.cp, 61.72.Qq

I. INTRODUCTION

Among the diluted magnetic semiconductors[1] Ge-based ones have recently attracted much attention, an interest stimulated by the possible compatibility with mature Si technology. Among these systems GeMn is most probably the so far best investigated[2–13] providing local ferromagnetic transition temperatures well above 100 K[7,9] and above room-temperature global ferromagnetic transition temperatures.[8,10]

A common approach to fabricate $Ge_{1-x}Mn_x$ layers on Ge substrates is the codeposition of Ge and Mn in low substrate temperature, solid source molecular-beam epitaxy (LT-MBE). Depending on the fabrication temperature it was found that for comparably high substrate temperatures $T_S \geq 120$ °C more than 99% of the codeposited Mn is incorporated in a high density of nanometer sized precipitates of the intermetallic phase Mn_5Ge_3.[6,9] Mn_5Ge_3 has a hexagonal crystal structure. The precipitates have either a partly coherent or an incoherent crystalline relationship with the Ge host lattice.[6] At sufficiently low substrate temperatures, in contrast, intermetallic precipitation can be suppressed and in turn apparently cubic, crystallographically fully coherent, nanometer sized areas with higher Mn content compared to the surrounding emerge.[7–9]

In this work, we provide further structural information on inclusions in MBE fabricated GeMn epilayers based on x-ray diffraction (XRD) methods. These methods probe much larger sample volumes as compared to the commonly used, locally sensitive transmission electron microscopy (TEM) and provide, in addition, accurate information on the strain state. We report on grazing-incidence diffraction (GID) experiments carried out with synchrotron radiation at the ESRF, Grenoble, France. From the GID experiments we not only determine the in-plane lattice constants of the $Ge_{1-x}Mn_x$ epilayers, but also measure the diffusely scattered intensities. Based on a theoretical description of diffuse x-ray scattering we derive the average in-plane inclusion radius as well as an estimate on the Mn concentration in the coherent clusters. Furthermore, by varying the incidence angle of the primary x-ray beam and hence the penetration depth, we get information of the Mn-rich inclusions as a function of the $Ge_{1-x}Mn_x$ layer thickness.

II. EXPERIMENT

We investigated three samples of epitaxial $Ge_{1-x}Mn_x$ layers fabricated by LT-MBE on Ge (001) substrates. Samples 1 and 2 were fabricated at $T_S=60$ °C with Mn contents of 3.4% and 8%, respectively. Sample 3 was fabricated at $T_S=120$ °C. For all samples, the $Ge_{1-x}Mn_x$ epilayer thickness was 200 nm and the Ge flux rate was 0.08 Å/s. Further details on sample fabrication are given in Refs. 6 and 7.

Superconducting quantum interference device (SQUID) magnetometry for samples with $T_S=60$ °C revealed no signature of known intermetallic GeMn phases. Instead signatures of local ferromagnetic transition temperatures of at least 160 K could be related to the nanometer sized areas with increased Mn content.[7] In the case of the sample with incoherent precipitates, below the ferromagnetic transition temperature of Mn_5Ge_3 at 296 K, superparamagnetism of the precipitates with a blocking temperature, which depends on the precipitate volume and thus on the fabrication parameters,[6] was observed.

We have also investigated the structure of all samples by TEM carried out in a Jeol 3010 microscope. It operates with an accelerating voltage of 300 kV reaching a point resolution of 0.18 nm. The TEM samples are prepared in cross-sectional and plan-view geometries. From the TEM results shown in Fig. 1 it follows that samples 1 and 2 [cf. Figs. 1(a)–1(d)] contain apparently Mn-rich inclusions coherently bound to the surrounding matrix.[7] For a Mn content of 3.4% (sample 1) the clusters have approximately the same extent in all three dimensions, while for 8% of Mn (sample 2), they are significantly elongated along the growth direction. The

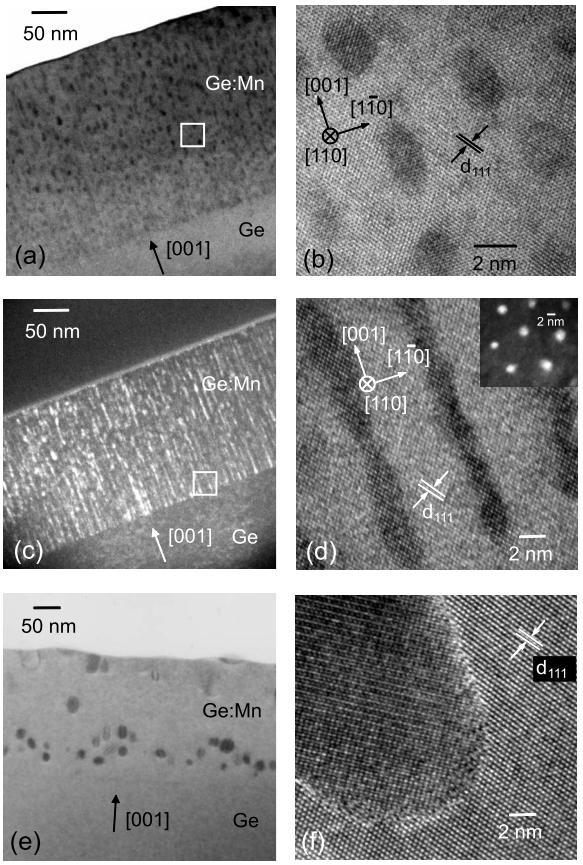

FIG. 1. TEM micrographs of sample 1 (3.4% Mn, growth temperature 60 °C), sample 2 (8.0% Mn, 60 °C), and sample 3 (3.4% Mn, growth temperature 120 °C). (a) Cross-sectional TEM bright-field TEM overview image of sample 1. Dark areas mark the Mn-rich inclusions being round shaped and coherently strained to the Ge matrix as indicated by the high-resolution TEM micrograph in (b). (c) Dark-field image of sample 2. The bright areas correspond to the Mn-rich coherent cluster, which are elongated along the [001] growth direction. (d) is the corresponding high-resolution image with inset showing a plan-view dark-field micrograph that demonstrates the circular shape of the inclusions with radius of 2–3 nm. (e) Bright-field cross-sectional image of sample 3; the corresponding high-resolution image is in (f).

TEM analysis confirms the presence of incoherent Mn_5Ge_3 precipitates in sample 3 [Figs. 1(e) and 1(f)].[6]

XRD experiments were carried out at the beamline ID01 at ESRF (Grenoble) using the x-ray energy of 6.54 keV. The scattered intensity was measured by a linear detector perpendicular to the sample surface. In most measurements, the diffracted intensity was collected over the whole detector window, so that we have integrated over the exit angles α_f in the range from 0° to approximately 2.2°. During the measurements the incidence angle α_i of the primary radiation was kept constant. α_i was chosen to be 0.3°, i.e., slightly below the critical angle α_c of total external reflection (0.38° for the energy used) or α_i=0.45°, yielding a penetration depth of about 10 nm and 1 μm, respectively. The distribution of the scattered intensity was measured along lines crossing the in-plane reciprocal-lattice points (RELPs) 220 or 400; these lines were parallel and perpendicular to the

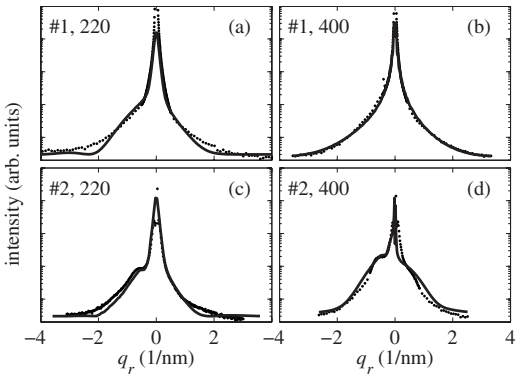

FIG. 2. Measured (dotted) and fitted (full lines) radial scans of samples 1 and 2 around the RELPs 220 and 400 with the incidence angle α_i=0.3°.

corresponding diffraction vector radial and angular intensity scans, respectively. In addition also the two-dimensional (2D) intensity distribution in the reciprocal plane parallel to the sample surface around 220 and 400 RELPs was measured using both incidence angles mentioned above. Measuring these maps, we have performed the α_f integration as well. For each sample and each value of α_i, two reciprocal-space maps were measured—close to the RELP and far from it.

The linear scans and the two-dimensional reciprocal-space maps for samples 1 and 2 with coherent inclusions are plotted in Figs. 2 and 3, whereas the linear scans and maps for sample 3 with incoherent precipitates are shown in Figs. 4 and 5. In addition in Fig. 6 the 2D intensity distribution in the close vicinity of the Ge 220 RELP for all three investigated samples is shown. In these figures, $q_{r,a}$ means the components of the reduced scattering vector $\boldsymbol{q}$ (see below) parallel and perpendicular to the diffraction vector $\boldsymbol{h}$, respectively.

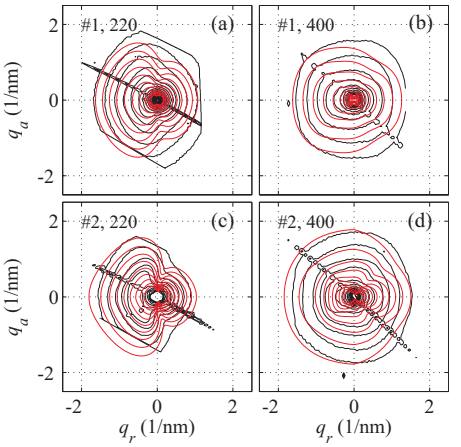

FIG. 3. (Color) Two-dimensional intensity maps of samples 1 and 2 measured (black) and calculated (red) in a broad range around the RELPs 220 and 400 with the incidence angle of 0.3°. The step of the intensity contours is $10^{0.2}$. The reciprocal $q_r q_a$ plane is parallel to the sample surface.

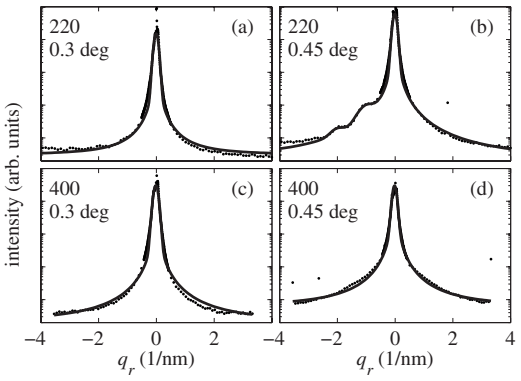

FIG. 4. Measured (dotted) and fitted (full lines) radial scans of sample 3 around the RELPs 220 and 400 with the incidence angles α_i=0.3° and 0.45°.

III. THEORETICAL: DIFFUSE X-RAY SCATTERING FROM SMALL INCLUSIONS

In this section we present the theoretical description of diffuse x-ray scattering from inclusions in an epitaxial layer and we discuss the method of how to determine the parameters of the inclusions from experimental data. The description is based on the kinematical approximation and on the theory of diffuse scattering in Ref. 14.

The intensity of x rays scattered with a given scattering vector $\boldsymbol{Q}=\boldsymbol{K}_f-\boldsymbol{K}_i$ ($\boldsymbol{K}_{i,f}$ are the wave vectors of the primary and scattered beams, respectively) is given by

$$I_{\boldsymbol{h}}(\boldsymbol{q}) = AN|F_{1\boldsymbol{h}}(\boldsymbol{q}) + F_{2\boldsymbol{h}}(\boldsymbol{q})|^2, \tag{1}$$

where $\boldsymbol{q}=\boldsymbol{Q}-\boldsymbol{h}$ is the reduced scattering vector, $\boldsymbol{h}$ denotes the diffraction vector (vector of the lattice reciprocal to the host lattice), A is a constant comprising the intensity of the primary wave and linear polarization factor, among others, N is the number of inclusions in the irradiated sample volume, and $F_{1,2\boldsymbol{h}}$ describe the waves scattered from the displacement field around an inclusion and from the inclusion core, respectively, where

$$F_{1\boldsymbol{h}}(\boldsymbol{q}) = \chi_{\boldsymbol{h}} \int_V d^3\boldsymbol{r} e^{-i\boldsymbol{q}\cdot\boldsymbol{r}}[e^{-i\boldsymbol{h}\cdot\boldsymbol{u}(\boldsymbol{r})} - 1] \tag{2}$$

and

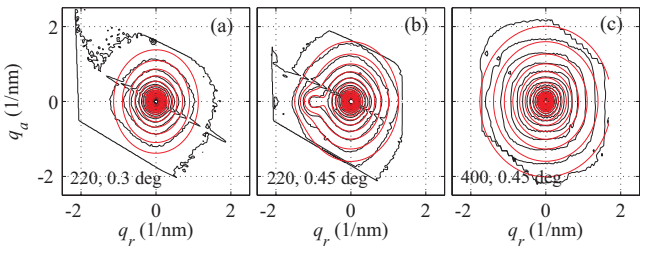

FIG. 5. (Color) Two-dimensional intensity maps of sample 3 measured (black) and calculated (red) in a broad range around the RELPs 220 and 400 with the incidence angles of 0.3° and 0.45°. The step of the intensity contours is $10^{0.2}$. The reciprocal $q_r q_a$ plane is parallel to the sample surface.

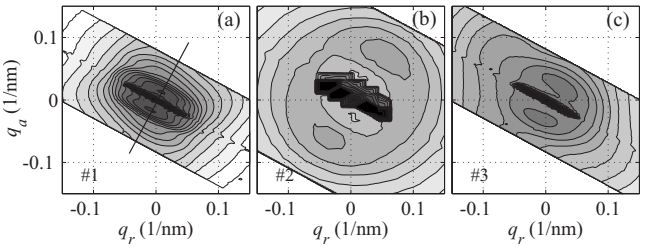

FIG. 6. Two-dimensional intensity maps of samples 1–3 measured in a small neighborhood of the RELP 220 with the incidence angle of 0.3°. The oblique line in the map of sample 1 denotes the trajectory of a linear scan used for the comparison with AFM data (see Fig. 8). The step of the intensity contours is $10^{0.2}$.

$$F_{2\boldsymbol{h}}(\boldsymbol{q}) = \Delta\chi_{\boldsymbol{h}} \int_V d^3\boldsymbol{r}\Omega(\boldsymbol{r}) e^{-i\boldsymbol{h}\cdot\boldsymbol{u}(\boldsymbol{r})}. \tag{3}$$

Here we have denoted V as the sample volume, $\boldsymbol{u}(\boldsymbol{r})$ is the displacement field around a single inclusion, $\Omega(\boldsymbol{r})$ is the shape function of the inclusion (unity in the inclusion volume and zero outside it), $\chi_{\boldsymbol{h}}$ is the $\boldsymbol{h}$th Fourier component of the polarizability of the host lattice, and $\Delta\chi_{\boldsymbol{h}}=\xi_{\text{incl}}\chi_{\boldsymbol{h}}$ is the difference of these components in the inclusion volume and around the inclusion. $\xi_{\text{incl}}\chi_{\boldsymbol{h}}$ is proportional to the relative difference in the average electron densities in the inclusion and in the host lattice. If the inclusion is incoherent (i.e., if it consists of a different crystallographic phase) close to a point of the lattice reciprocal to the host lattice the inclusion volume does not diffract and $\Delta\chi_{\boldsymbol{h}}=-\chi_{\boldsymbol{h}}$.

Equations (1)–(3) have been derived assuming that (i) the positions of the inclusions are completely noncorrelated, (ii) the scattering process is fully kinematical, i.e., multiple scattering is neglected, and (iii) the inclusions are homogeneously distributed in the sample volume. The validity of approximation (i) has been proven by cross-sectional and plan-view TEM of the investigated samples that did not reveal any significant correlation in the inclusion positions (see Fig. 1).[6,7]

The kinematical approximation (ii) is not justified since in grazing-incidence scattering geometry x-ray reflection and refraction at the sample surface z=0 must be considered. This can be taken into account by replacing the reduced scattering vector $\boldsymbol{q}=(\boldsymbol{q}_\parallel, q_z)$ by its value $\boldsymbol{q}_T$ corrected to refraction and absorption

$$\boldsymbol{q}_T = (\boldsymbol{q}_\parallel, q_{Tz}), \quad q_{Tz} = k_{fz} - k_{iz} - h_z,$$

where $k_{i,fz}$ are the vertical components of the wave vectors of the primary and scattered beams corrected to refraction

$$k_{i,fz} = \mp K\sqrt{\sin(\alpha_{i,f})^2 - 2\delta},$$

$K=2\pi/\lambda$ is the wave vector in vacuum, $\alpha_{i,f}$ are the angles of incidence and exit, $\delta=1-n$ (in this formula, n is the refraction index of the substrate), and the z axis is parallel to the outward surface normal. In addition, the scattered intensity is multiplied by the term $|t_i t_f|^2$ containing the Fresnel transmission coefficients of the free surface for the primary and scattered beams.[15]

TABLE I. $Ge_{1-x}Mn_x$ samples with their fabrication and fit parameters. x represents the nominal average Mn content, T_S the MBE fabrication temperature, and Mn incorporation the type of inclusions present in the sample. The fit parameters are R_{incl}, being the average inclusion radius, ξ_{incl} the relative lattice polarizability, f_{incl} the relative lattice misfit between inclusion and surrounding Ge host, and x_{incl} the average Mn content within the inclusions.

Sample	x (%)	T_S (°C)	Mn incorporation	R_{incl} (nm)	ξ_{incl}	f_{incl}	x_{incl} (%)
1	3.4	60	Mn-rich clusters	1.7 ± 0.4	-0.1 ± 0.03	-0.01 ± 0.003	~ 7
2	8	60	Mn-rich clusters	2.2 ± 0.3	-0.3 ± 0.05	-0.02 ± 0.005	~ 20
3	120	120	Mn_5Ge_3 precipitates	8 ± 2	-1	<0.001	—

If the inclusions are distributed only in a thin surface layer, the assumption (iii) is not valid. In this case, the displacement field around the inclusion is affected by the surface stress relaxation so that the displacement in point $\boldsymbol{r}$ from an inclusion in point $\boldsymbol{r}'$ depends also on the depth z' of the inclusion below the surface ($z'<0$), i.e., $\boldsymbol{u}(\boldsymbol{r}-\boldsymbol{r}';z')$. Then, Eq. (1) has to be modified to[16,17]

$$I_{\boldsymbol{h}}(\boldsymbol{q}) = A \int_{-\infty}^{0} dz' N(z') |F_{1\boldsymbol{h}}(\boldsymbol{q};z') + F_{2\boldsymbol{h}}(\boldsymbol{q};z')|^2, \qquad (4)$$

where $N(z')$ is the number of inclusions in the depth z' below the free surface.

In our experiments we have integrated the scattered intensity over a certain range of the exit angles α_f; this integration can be approximately expressed by the integration of the simulated intensity over q_z. Including all the above improvements, the measured signal is given by

$$J_{\boldsymbol{h}}(\boldsymbol{q}_{\parallel}) = A \int_{-\infty}^{0} dz' N(z') \int_{S} dq_z |t_i t_f|^2 C(\boldsymbol{q}_T) |F_{1\boldsymbol{h}}(\boldsymbol{q}_T;z') + F_{2\boldsymbol{h}}(\boldsymbol{q}_T;z')|^2. \qquad (5)$$

The factor $|t_i t_f|^2$ exhibits a sharp maximum for $q_z=q_{zc}$, for which the exit angle α_f equals the critical angle α_c (so-called Yoneda wing[15]). Therefore, for a rough estimate of the scattered intensity, the integral $\int_S dq_z$ can be neglected and the measured signal can be approximated by the value $I_{\boldsymbol{h}}(\boldsymbol{q}_{\parallel}, q_{zc})$.

For the calculation of the factor $F_{1\boldsymbol{h}}(\boldsymbol{q};z')$ we have to evaluate the displacement field $\boldsymbol{u}(\boldsymbol{r}-\boldsymbol{r}';z')$ in point $\boldsymbol{r}$ caused by an inclusion in point $\boldsymbol{r}'$. In many works on diffuse x-ray scattering, an asymptotic expression for the displacement field in an infinite crystal matrix is used,[18,19] in which the displacement vector depends only on $\boldsymbol{r}-\boldsymbol{r}'$ and its magnitude is proportional to $|\boldsymbol{r}-\boldsymbol{r}'|^{-2}$. In our case, however, this simplified approach cannot be used for two reasons: (i) The diffusely scattered intensity in points $\boldsymbol{q}$ in reciprocal space, for which $|\boldsymbol{q}| > 2\pi/R_{\mathrm{incl}}$ (R_{incl} is the inclusion radius), depends mainly on the displacement field in a close vicinity of the inclusion. Here the asymptotic formula is not valid.[14] (ii) In order to enhance the intensity scattered from the defects we used grazing-incidence diffraction with the incidence angle of the primary x-ray beam close to the critical angle of total external reflection. In this geometry, the penetration depth of the primary beam L is rather small and the displacement field of an inclusion close to the surface is affected by surface stress relaxation, which is not taken into account in the asymptotic formula. For these reasons we calculated the displacement field of an inclusion *exactly*, using the continuum elasticity approach and the Fourier method.[15]

Numerical simulations showed that the shape of the concentration profile $N(z')$ of the inclusions across the GeMn layer has almost no influence on the measured scans $J(\boldsymbol{q}_{\parallel})$, and consequently a constant concentration profile of the inclusions was assumed in the whole GeMn layer in the simulations.

IV. RESULTS AND DISCUSSION

In order to extract quantitative information from the measurements, the intensity distributions measured in angular and radial directions were fitted using Eq. (5). Three inclusion parameters were determined, namely, (i) the in-plane inclusion radius R_{incl} assuming a circular in-plane shape of the inclusions, (ii) the relative difference ξ_{incl} in the average electron densities per unit cell in the inclusion and in the host lattice [from $\Delta\chi_{\boldsymbol{h}}$ in Eq. (3)], and (iii) the effective mismatch $f_{\mathrm{incl}}=(a_{\mathrm{inclusion}}-a_{\mathrm{matrix}})/a_{\mathrm{matrix}}$, corresponding to the relative difference of the *relaxed* lattice parameters of the Mn-rich inclusion and Ge host lattice. No misfit dislocations are present on the interface between the Ge substrate and the $Ge_{1-x}Mn_x$ layer, so that the lateral lattice parameter of the solid solution $a_{\mathrm{matrix}\parallel}$ surrounding the inclusions equals the lattice parameter of the Ge substrate underneath and it is therefore completely not affected by possibly diluted Mn atoms. The reciprocal-space distributions of the diffusely scattered intensity in the $q_r q_a$ plane parallel to the sample surface are completely not sensitive to the diluted Mn atoms; they also do not depend on the inclusion size perpendicular to the surface.

We first determine R_{incl} by fitting the measured angular scans (not shown) using Eq. (5) since the shape of these scans is almost independent of the other parameters ξ_{incl} and f_{incl}. Then, we keep R_{incl} fixed and determine ξ_{incl} and f_{incl} from the radial scans again using Eq. (5). The fitted scans are plotted in Figs. 2 and 4. Finally, using the parameter values determined from the linear scans we calculated the 2D intensity maps $J(\boldsymbol{q}_{\parallel})$. Figures 3 and 5 compare the measured and simulated 2D intensity maps. The parameters following from all fits are summarized in Table I.

The intensity distribution of samples 1 and 2 with coherent Mn-rich inclusions shows no dependence on the incidence angle α_i suggesting a uniform distribution of the co-

herent clusters over the GeMn layer thickness. The fits of the angular scans of these samples (not shown) provide $R_{\mathrm{incl}}=1.7\pm0.4$ nm for the sample with 3.4% Mn and $R_{\mathrm{incl}}=2.2\pm0.3$ nm for the sample with higher Mn content, in good agreement with TEM results shown in Fig. 1. In the radial scan direction, for which the scattered intensity is sensitive to the in-plane strain, the coherent clusters show a distinct asymmetry in the intensity distribution at lower q_r values, best visible in the scans around 220 RELP (see Fig. 2). This asymmetry is also clearly depicted in the 2D intensity distribution around the 400 and 220 RELPs (see Fig. 3). The location of the maximum of the diffusely scattered intensity at lower q_r with respect to the Ge RELP can only be caused by an enlarged Ge lattice constant, i.e., by a *tensily* strained Ge lattice in the vicinity of the Mn-rich clusters. For coherent cubic clusters the tensile strain in turn indicates the lattice constant of the cluster regions to be smaller than the surrounding Ge host lattice, i.e., the mismatch f_{incl} is negative.

The asymmetry in the radial scans is stronger for sample 2 with higher total Mn content (8%) compared to sample 1 with 3.5% Mn. It follows that the Mn clusters in sample 2 have a smaller lattice constant than the ones in sample 1. This indicates that in the sample with the higher total Mn content also more Mn is incorporated within the Mn-rich clusters.

The quantification of the lattice mismatch f_{incl} is complicated by the fact that the scattered intensity is affected mainly by the distortion of the host lattice in the vicinity of the inclusions and the influence of the inclusion volume is rather small. Therefore, the values of the mismatch parameter f_{incl} extracted from the scattering data by fitting to Eq. (5) determine the elastic deformation of the host lattice around the cluster, rather than the true lattice parameter of the inclusion. If the inclusion lattices were distorted, the displacement field around the inclusion would also depend on the nature of the inclusion and only an effective value of f_{incl} could be determined.

The resulting mismatch values of f_{incl} are summarized in Table I. They are in good agreement with estimations from electron microscopy reported for comparable self-assembled Mn-rich regions.[8] However, the mismatch values are significantly larger than values known for pseudomorphically fabricated magnetic semiconductors without self-assembled Mn-rich regions such as (Ga,Mn)As.[20] Since the large lattice mismatch in the Mn-rich areas would involve a strain relaxation mechanism beyond a certain critical size, the measured f_{incl} values thus might account for the fact that so far no Mn-rich regions with diameters beyond a few nanometers have been found.[3,7–9]

The parameter ξ_{incl}, the relative change in the lattice polarizability, depends on the local density x_{incl} of Mn ions in the inclusions. However, this dependence is difficult to establish since the lattice polarizability depends also on the local lattice distortion and lattice defects around the Mn ions and on their crystallographic positions. If we neglect distortion and defects, and assume that all Mn atoms are in lattice positions, $x_{\mathrm{incl}}\approx-0.67\xi_{\mathrm{incl}}$. We emphasize that this relationship is a very rough approximation and should rather serve as a lower limit for the Mn content within the inclusion. Fitting the radial scans yields $x_{\mathrm{incl}}=7\%$ and 20% for samples 1 and 2, respectively. These lower limits for the Mn content are in the same order of magnitude as hitherto observed values ranging from 10% to approximately 38%.[3,7,8] The results confirm that offering an overall higher Mn flux during MBE growth also results in a higher x_{incl} content within the coherent cubic clusters.

Applying the fitting procedure described above to the sample with incoherent precipitates, $R_{\mathrm{incl}}=8\pm2$ nm was extracted from the angular scans. This value agrees well with the previously reported $R_{\mathrm{incl}}\approx7$ nm observed in TEM analysis (see also Fig. 1 and Ref. 6). The radial scans depicted in Fig. 4 show a prominent feature on the left-hand side of the main maximum, which is only visible at incidence angles $\alpha_i=0.45°$ corresponding to a penetration depth of ~1 μm, but not for a penetration depth of ~10 nm ($\alpha_i=0.35°$). This is also clearly depicted in the 2D intensity maps of sample 3 at different α_i in Fig. 5, where with larger incidence angle a distinct side maximum can be seen. This maximum corresponds to the (300) diffraction peak from the hexagonal Mn_5Ge_3 phase. The fact that this maximum occurs only for larger incidence angle (i.e., for larger penetration depths of the primary x-ray beam) coincides with the TEM results depicted in Fig. 1, where the incoherent inclusions do not occur close to the top sample surface but are rather located close to the substrate-layer interface. The width of the 300 Mn_5Ge_3 diffraction peak in the radial scans of Fig. 4 agrees with the value determined from the angular scans and thus also with the TEM results.

Both radial scans in Fig. 4 and the diffusely scattered intensity around the RELP of the host lattice in Fig. 5 exhibit *no* asymmetric shape indicating only little deformation of the inclusion neighborhood. Since the inclusions in sample 3 have a completely different crystal structure compared to the surrounding, the value of f_{incl} *cannot* be interpreted as a relative difference of the lattice parameters of the inclusion and the host lattice, but only as a numerical constant determining the elastic deformation of the host lattice around an inclusion. Therefore the mismatch f_{incl} of sample 3 had to be estimated from the comparison of the measured and simulated intensity maps shown in Fig. 5. The obtained low value of $f_{\mathrm{incl}}<0.1\%$ confirms that the incoherent Mn_5Ge_3 precipitates almost do not result in a deformation of the Ge host lattice. Apparently, the lattice incoherence or only a partial crystallographic relationship with the Ge host lattice gives rise to an almost complete strain relaxation.

Due to a large difference in the crystal structure of the incoherent inclusion and of the host lattice, the inclusion volumes can be considered as empty holes around the RELPs 220 and 400 of the host lattice, having $\Delta\chi_{\boldsymbol{h}}=-\chi_{\boldsymbol{h}}$ and $\xi_{\mathrm{incl}}=-1$. Therefore, no information on the difference between the average electron densities in the inclusion and in the host lattice and thus no estimation of the Mn content x_{incl} within the precipitates can be deduced from the measurements.

The comparison of the simulated maps with the measured ones of all samples in a wide $\boldsymbol{q}_{\parallel}$ range is shown in Figs. 3 and 5. The simulations of the linear scans and of the 2D intensity maps agree well with the experimental data, confirming that the assumed model properly describes the inclusion of coherent clusters and incoherent precipitates in the Ge host lattice.

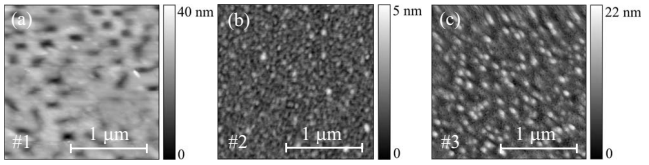

FIG. 7. AFM pictures of the surfaces of samples 1–3.

The good agreement between the simulated and measured reciprocal-space maps including the (300) Mn_5Ge_3 hexagonal precipitate peak is achieved by summing up the contribution of the diffuse intensity distribution excited by "holes" in the Ge lattice and of the intensity directly scattered by the precipitates, respectively [see Fig. 5(b)].

In spite of the very good agreement of the measured and simulated intensities, in close vicinity of the measured RELPs side maxima emerge that cannot be explained by our inclusion model. These side maxima are better displayed in Fig. 6 showing the 2D maps measured in a close vicinity of the RELP 220. The elongation of the maxima in the direction perpendicular to the diffracted beam (i.e., making the Bragg angle with the q_r axis) is explained by the anisotropic resolution function for the given experimental conditions. In the direction perpendicular to the primary beam the resolution is much better than in the direction perpendicular to the scattered beam. In the former direction the resolution is determined by the angular divergence of the primary beam (few seconds of arc), while in the latter it depends on the width of the entrance detector slit, yielding the angular resolution of about 50 s of arc. In order to explain the nature of these side maxima, we have to consider the fact that GID is also a surface sensitive technique. Therefore, additional features in intensity maps are not necessarily correlated with subsurface structural properties, but to the morphology of the sample surface. In order to prove this effect, the surface morphology of all samples was investigated with atomic force microscopy. Figure 7 shows the atomic force microscopy (AFM) pictures of the three samples investigated. The Fourier transformation of the surface morphology was then calculated and its square compared to linear GID scans across the side maxima extracted from Fig. 6. This comparison is shown in Fig. 8. The good agreement between the curve shapes of Fourier transformed surface morphology and linear scans supports the hypothesis that the side maxima in the intensity distribution of the reciprocal-space maps can indeed be explained by surface corrugations of the samples.

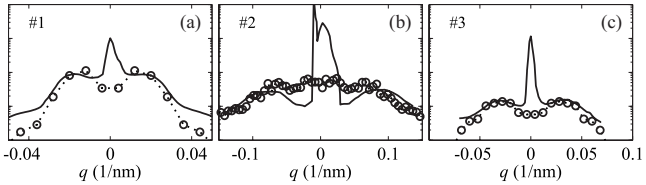

FIG. 8. Comparison of the Fourier transformation of the AFM data (points) with the line scans extracted from the reciprocal-space maps shown in Fig. 6 (lines).

V. CONCLUSION AND SUMMARY

In this work, we have shown that the combination of synchrotron x-ray diffraction experiments in grazing-incidence geometry with an appropriate scattering theory is a suitable tool to investigate the influence of magnetic impurities in a semiconductor host material such as in GeMn on its structural properties. Both inclusions of apparently coherent Mn-rich regions and incoherent Mn_5Ge_3 precipitates in a diamond lattice Ge host were investigated. Incoherent Mn_5Ge_3 precipitates induce almost no elastic in-plane strain on the Ge lattice, indicating strain relaxation in the crystallographically incoherent interface of an inclusion and the host lattice due to the significantly different crystal structures of inclusions and host lattice. In contrast, the coherent Mn-rich regions impose significant elastic in-plane strain on the matrix resulting in lattice mismatches $\geq 1\%$. Such large strain values could be a driving force for the observed self-assembly of Mn-rich regions and appear to be one of the limiting factors of the in-plane Mn-rich region diameter. Size and average Mn content of the apparently coherent regions were also determined and were found to increase with increasing overall Mn content.

ACKNOWLEDGMENTS

This work is a part of the research program MSM 0021620834 that is financed by the Ministry of Education of the Czech Republic. We acknowledge the financial support of the Grant Agency of the Czech Republic (Project No. 202/06/0025) and of the Austrian Science Fund FWF (Project No. P18942-N20). We also acknowledge funding from the German Science Foundation (DFG) via Schwerpunktprogramm SPP 1285 Halbleiter Spintronik under Projects No. 1 and No. 55. The XRD experiments were performed at the beamline ID01 at the ESRF in Grenoble, France.

[1] T. Dietl and H. Ohno, Mater. Today **9**, 18 (2006).
[2] Y. D. Park, A. T. Hanbicki, S. C. Erwin, C. S. Hellberg, J. M. Sullivan, J. E. Mattson, T. F. Ambrose, A. Wilson, G. Spanos, and B. T. Jonker, Science **295**, 651 (2002).
[3] A. P. Li, C. Zeng, K. van Benthem, M. F. Chisholm, J. Shen, S. V. S. Nageswara Rao, S. K. Dixit, L. C. Feldman, A. G. Petukhov, M. Foygel, and H. H. Weitering, Phys. Rev. B **75**, 201201(R) (2007).
[4] C. Bihler, C. Jaeger, T. Vallaitis, M. Gjukic, M. S. Brandt, E. Pippel, J. Woltersdorf, and U. Gösele, Appl. Phys. Lett. **88**, 112506 (2006).
[5] C. Jaeger, C. Bihler, T. Vallaitis, S. T. B. Goennenwein, M. Opel, R. Gross, and M. S. Brandt, Phys. Rev. B **74**, 045330 (2006).
[6] S. Ahlers, D. Bougeard, N. Sircar, G. Abstreiter, A. Trampert, M. Opel, and R. Gross, Phys. Rev. B **74**, 214411 (2006).
[7] D. Bougeard, S. Ahlers, A. Trampert, N. Sircar, and G. Abstre-

iter, Phys. Rev. Lett. **97**, 237202 (2006).
[8] M. Jamet, A. Barski, T. Devillers, V. Poydenot, R. Dujardin, P. Bayle-Guillemaud, J. Rothman, E. Bellet-Amalric, A. Marty, J. Cibert, R. Mattana, and S. Tatarenko, Nature Mater. **5**, 653 (2006).
[9] T. Devillers, M. Jamet, A. Barski, V. Poydenot, P. Bayle-Guillemaud, E. Bellet-Amalric, S. Cherifi, and J. Cibert, Phys. Rev. B **76**, 205306 (2007).
[10] C. Zeng, Z. Zhang, K. van Benthem, M. F. Chisholm, and H. H. Weitering, Phys. Rev. Lett. **100**, 066101 (2008).
[11] J.-P. Ayoub, L. Favre, I. Berbezier, A. Ronda, L. Morresi, and N. Pinto, Appl. Phys. Lett. **91**, 141920 (2007).
[12] P. De Padova, J. P. Ayoub, I. Berbezier, P. Perfetti, C. Quaresima, A. M. Testa, D. Fiorani, B. Olivieri, J. M. Mariot, A. Taleb-Ibrahimi, M. C. Richter, O. Heckmann, and K. Hricovini, Phys. Rev. B **77**, 045203 (2008).
[13] N. Pinto, L. Morresi, M. Ficcadenti, R. Murri, F. D'Orazio, F. Lucari, L. Boarino, and G. Amato, Phys. Rev. B **72**, 165203 (2005).
[14] M. A. Krivoglaz, *X-Ray and Neutron Diffraction in Nonideal Crystals* (Springer, Berlin, 1996).
[15] U. Pietsch, V. Holý, and T. Baumbach, *High-Resolution X-Ray Scattering from Thin Films to Lateral Nanostructures* (Springer, Berlin, 2004).
[16] R. I. Barabash and M. A. Krivoglaz, Fiz. Tverd. Tela (Leningrad) **29**, 3081 (1987).
[17] V. B. Molodkin, S. I. Olikhovskii, and M. E. Osinovskii, Phys. Met. Metallogr. **5**, 1 (1984).
[18] H. Trinkaus, Phys. Status Solidi B **51**, 307 (1972).
[19] H. Trinkaus, Phys. Status Solidi B **54**, 209 (1972).
[20] H. Ohno, J. Magn. Magn. Mater. **200**, 110 (1999).